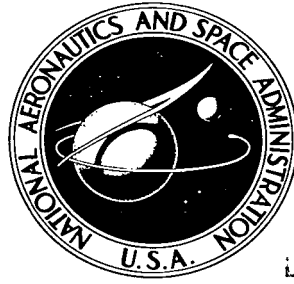


NASA TECHNICAL NOTE



NASA TN D-3963

2.1

1

LOAN COPY: RET
AFWL (WLI)
KIRTLAND AFB,



NASA TN D-3963

STIFFNESS MATRIX SOLUTION FOR
SHELLS OF REVOLUTION POSSESSING
VARIABLE THICKNESS HEAT PROTECTION

by Frederick Jean Stebbins
Manned Spacecraft Center
Houston, Texas



STIFFNESS MATRIX SOLUTION FOR SHELLS OF REVOLUTION
POSSESSING VARIABLE THICKNESS HEAT PROTECTION

By Frederick Jean Stebbins

Manned Spacecraft Center
Houston, Texas

NATIONAL AERONAUTICS AND SPACE ADMINISTRATION

For sale by the Clearinghouse for Federal Scientific and Technical Information
Springfield, Virginia 22151 - CFSTI price \$3.00

ABSTRACT

The Apollo command module aft heat shield, a composite laminated torispherical shell, was idealized as a network of curved beams. A stiffness matrix method was developed in torispherical coordinates to analyze the structural model for thermal and mechanical loadings. Correlation of the analytical method was demonstrated with a closed-form solution of the Apollo aft heat shield under a cold-soak thermal condition. Analyses of the structure were also correlated with data from a static test.

STIFFNESS MATRIX SOLUTION FOR SHELLS OF REVOLUTION POSSESSING VARIABLE THICKNESS HEAT PROTECTION

By Frederick Jean Stebbins
Manned Spacecraft Center

SUMMARY

A composite laminated torispherical shell was idealized as a network of curved beams. A stiffness matrix method was developed to analyze the structural model. The method was developed in torispherical coordinates which are amenable to the current family of manned spacecraft. The laminated shell was composed of an ablator, a bond, two stainless-steel face sheets, and a 2-inch-thick stainless-steel core.

A structural model of the Apollo aft heat-shield substructure was analyzed for a variety of thermal and mechanical loadings. A correlation was made of the analysis with test data and two independent digital computer analyses. An analysis of a symmetrical model of the Apollo aft heat shield under cold-soak conditions was compared with a closed-form solution to establish a link with "exact" theory. Selected stresses and displacements were used in the comparisons to demonstrate the accuracy of the procedure.

INTRODUCTION

The high strength-to-weight ratio of shells has been effectively utilized in spacecraft design. Elements of the common shells of revolution, that is, spheres, cylinders, tori, and cones, are assembled into spacecraft structural shapes. The Apollo spacecraft, for example, is a contiguous assembly of two spherical sections, a truncated cone and a toroidal section. Hyperthermal conditions during reentry require a heat-protective system surrounding the structural shell. For heat protection, the United States spacecraft have commonly had a variable thickness ablative material which forms a nonstructural char during reentry. The mechanical properties of the ablator in the virgin state are highly temperature-dependent. Contemporary spacecraft design features a stainless-steel sandwich substrate. The ablator and substrate form a complex laminated shell which is rotationally and meridionally asymmetric.

The structural design of spacecraft presents many interrelated problem areas. At the time of maximum dynamic loading during the launch phase, the solution to the problem involves more than static-load considerations. The dynamic mode shapes of the spacecraft must be established and the possibility of buffeting investigated. The translunar and reentry flight phases present two opposite extremes in thermal loading.

The operation of thermally deformed hatches is also a problem. These hatch doors must be used during the mission for extravehicular activity by the astronauts and for operation of equipment such as the astro sextant. The fiery reentry phase places extreme requirements on the spacecraft materials; however, the actual landing creates more structural problems than any other phase of the spaceflight mission. These structural problems of landing begin with the jolt of the arresting parachutes. Even though landing represents the terminal phase of the mission, it is most important that the watertight integrity of the spacecraft be maintained since the spacecraft must float until it is recovered.

The requirements imposed by aerodynamic considerations have resulted in geometric shapes which are not structurally desirable. In the cases of the Mercury, Gemini, and Apollo vehicles, the structure of the spacecraft has involved a prominent torispherical section. From the viewpoint of the structural engineer, it is desirable that the radius of the spherical area be small in order to minimize the water impact during landing. However, aerodynamic stability requirements necessitate a relatively large spherical radius. The necessary compromise between aerodynamic and structural objectives emphasized the need for accurate structural analysis.

Most of the analytical work in this area has been confined to the studies of shells of revolution (refs. 1 to 5). The objective of the research presented in this report was to develop a method of static structural analysis for a class of asymmetric shells subjected to arbitrary loads and temperatures. The thermal loads were limited to inplane forces and moments having vectors that are tangent to the shell midsurface. The thermal gradient may be arbitrary in the thickness direction of the shell and the surface coordinates. The shell may have variable meridional and circumferential stiffness properties. Since spacecraft, as well as airplanes, have a plane of symmetry relative to the flight path (fig. 1), the attendant reduction of unknowns was made. The application of the present method of static structural analysis of asymmetric shells under arbitrary loading was made to the Apollo aft heat-shield substructure. Theoretical and experimental correlation is demonstrated.

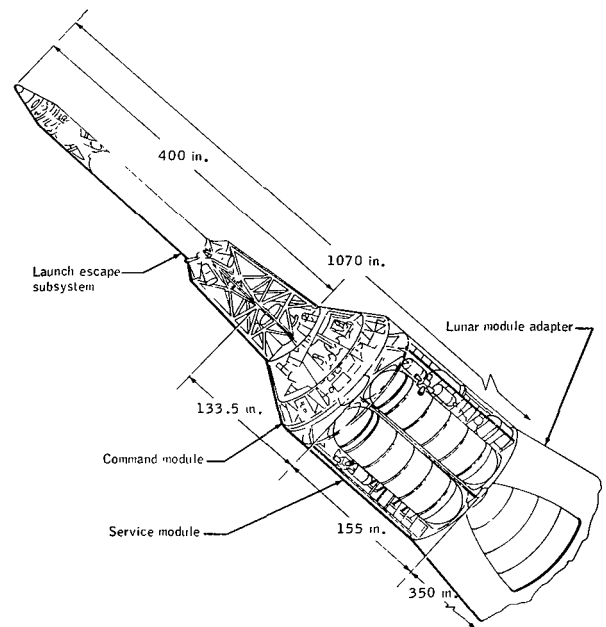


Figure 1. - Apollo spacecraft.

SYMBOLS

A	one end of the structural element AB
$\left. \begin{matrix} A_{AB}, A'_{AB}, A_{BA}, \\ A'_{BA}, A_{B'B}, A_{0A} \end{matrix} \right\}$	transformation matrices of the typical structural element, that is, A_{ij} is the transform from end j to end i (ref. 6)
B	one end of the structural element AB
b_θ, b_φ	beam width normal to θ or φ direction, in.
C	constants C_1 to C_{16} as used in table A-I
d_i	distance from the centroid of composite structure to ith laminate, in.
E	modulus of elasticity, psi
f_{BB}	flexibility matrix of the typical structural element for end A fixed and end B free
G	modulus of rigidity, psi
I	moment of inertia, in ⁴
J_e	geometrical torsion constant, in ⁴
\bar{k}	joint stiffness matrix
k_{AA}, k_{BB}	stiffness submatrices of the typical structural element for end B fixed and end A free, and for end A fixed and end B free, respectively (ref. 6)
k_{AB}, k_{BA}	stiffness submatrices of the coupling actions at end A due to displacements at end B, or for coupling actions at end B due to displacements at end A (ref. 6)
k^{AB}	total stiffness matrix of the member AB
P_1, P_2, P_3	force in R, φ , and θ directions, respectively, lb
P_4, P_5, P_6	moment about R, φ , and θ axes, respectively, in-lb

p_A, p_B	column vectors of internal actions at end A and at end B respectively, of a structural element AB
p_{BA}, p_{BB}	column vectors of actions at end B due to loads at end A and at end B
p_{A0}, p_{B0}	column vectors of applied actions at end A and at end B of a structural element AB
p_i	group of action components p_1 to p_6 (ref. 6)
p_o	externally applied load to beam AB, lb or in-lb
R, R_1, R_2	linear torispherical coordinates of sphere, of torus, and of torus reference ring, respectively, in.
\bar{R}	R value at joint centroid, $\bar{R} = \Delta R + R_B$ (fig. 6), in.
r	radius, in.
S	cross-sectional area, in ²
T	temperature, °F
T_o	zero stress temperature of composite structure, °F
t	thickness, in.
u_1, u_2, u_3	displacement in R, φ , and θ directions, respectively, in.
u_4, u_5, u_6	rotation about R, φ , and θ axes, respectively, rad
u_A, u_B	column vectors of internal displacements at end A and at end B
u_{B0}, u_{A0}	column vectors of applied displacements at end B and at end A
u_i	group of joint displacement components u_1 to u_6 (ref. 6)
α	coefficient of thermal expansion, in/in/°F
γ_1, γ_2	mechanically equivalent thermal load parameters (defined by eqs. 18 and 19)
θ	angular torispherical coordinate, deg

ν	Poisson ratio
ρ_c	density of core material, lb/in ³
ρ'_c	gross core density, lb/in ³
σ_φ	meridional stress, psi
φ	angular torispherical coordinate, deg

Subscripts:

a	ablator
b	bond
c	core (moduli based on gross cross section)
e	equivalent
fp	faceplate
i	the ith laminate
j	joint
n	the nth laminate
R, φ, θ	torispherical coordinates
s	substrate

THEORY

Structural Idealization

It was assumed that plane stress conditions existed in the class of laminated shells under investigation. The heat-protective material had a thermal gradient through its thickness. The temperature-dependent mechanical properties of the ablator were represented by multiple laminates, each at a constant temperature (fig. 2). Additional laminates were used to represent a bond layer and the elements of the sandwich construction. The temperature gradient through the shell thickness was represented in a step-function manner in which each of the laminates of figure 2 was at a specific temperature (fig. 3). The shell structure was idealized by a network of curved beams (fig. 4).

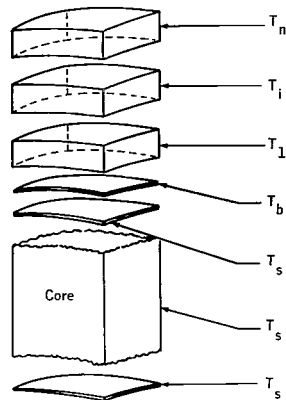


Figure 2. - Exploded view of composite structure.

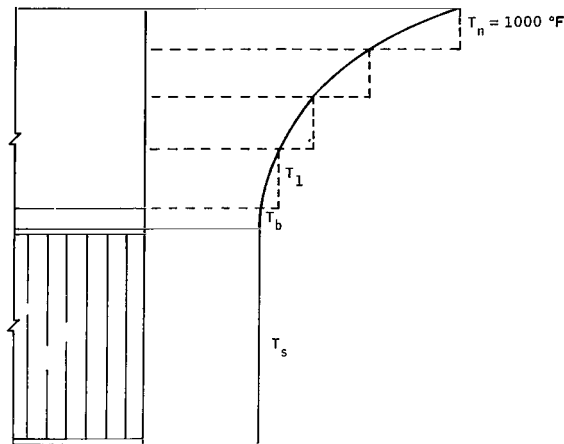


Figure 3. - Temperature distribution with step functions in the R direction.

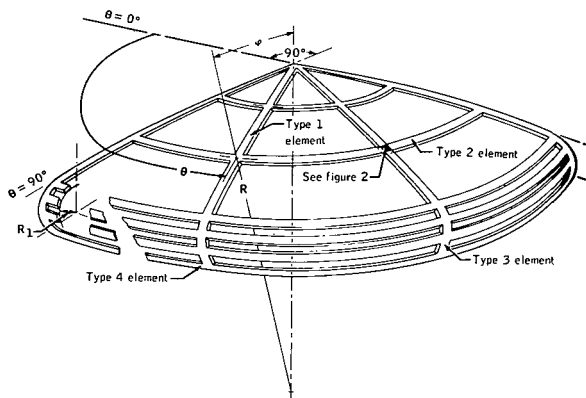


Figure 4. - Structural idealization of the Apollo aft heat shield.

The torispherical shell, idealized in figure 4, is the general structural shape used in the theoretical development of the present research; however, a similar approach could be followed for other shapes. The theoretical development of the stiffness matrix for the typical beam element is presented in appendix A, and the necessary transformations appear in appendix B.

Coordinate System

A torispherical coordinate system was used to define the geometry of the structural model shown in figure 4. In the spherical coordinate system, a point in space is described by its distance and direction from a fixed reference point. The coordinates are R , φ , and θ , which represent a distance and two angles, respectively. Torispherical coordinates have the same two surface coordinates φ and θ , but the coordinate R must be redefined as $R = f(R_1, R_2)$, in which R_1 is the torus radius measured from the torus reference ring and R_2 is the distance from the reference point to the loci of points describing the torus reference ring. If R_1 is set equal to zero, the torispherical coordinate system is reduced to the more familiar spherical coordinate system.

Procedure

A stiffness matrix method was followed. In the formulation of the procedure, it was necessary to obtain the stiffness matrix of the typical structural element. Since a flexibility matrix was easier to obtain, the stiffness matrix was determined by the inversion of the appropriate flexibility matrix (ref. 6). In matrix notation, this may be expressed as $k_{BB} = f_{BB}^{-1}$. The flexibility matrix was assembled through the application of the method of consistent distortion (see fig. 5 and appendix A for the development of the flexibility matrix f_{BB}). In general, a displacement at one end of the

NASA-S-66-11549 DEC 6

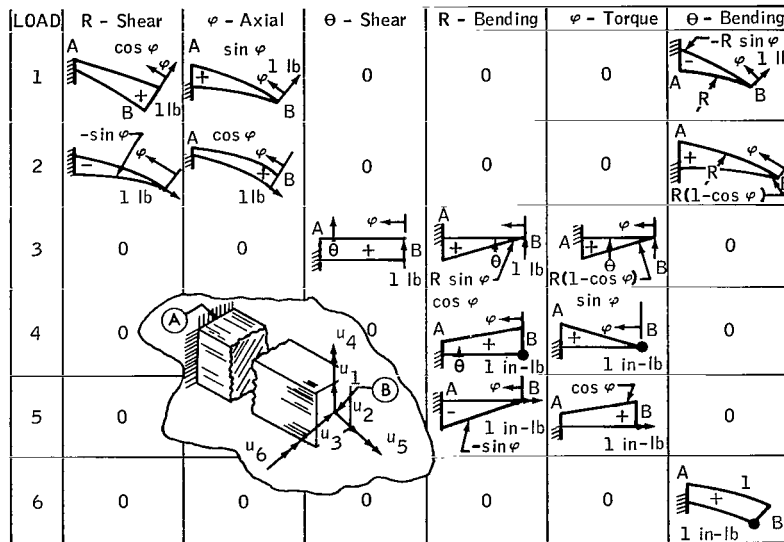


Figure 5. - Unit loadings for influence coefficients to type 1 beam elements.

typical structural element will cause actions to be realized at both ends of the element. These actions are shear force normal to the shell midsurface, axial force tangent to the shell midsurface, shear force tangent to the shell midsurface, bending moment normal to the shell midsurface, torsional moment, and bending moment tangent to the shell midsurface. If the typical structural element AB, fixed at end A, undergoes a unit displacement at end B, six actions occur at end A and six actions occur at end B. Thus, k_{BB} is obtained through successive unit displacements at end B while end A is held in a fixed condition. A coupling stiffness matrix k_{AB} relates the actions at end A due to unit displacements at end B. The total stiffness matrix for a member AB is

$$k^{AB} = \begin{bmatrix} k_{AA} & k_{AB} \\ k_{BA} & k_{BB} \end{bmatrix} \quad (1)$$

elements were oriented with joint φ coordinate direction, and type 2 and type 4 beam elements were oriented with the joint θ coordinate direction. A transformation of type 2 beam element actions was required so that the actions might be expressed as functions of the joint coordinates. A similar relationship was true between type 3 and type 4 beam elements. Joints occurring on the outer toroidal boundary were loaded by three members instead of four. The joint in which the most complex transformation arose was the joint located at $\bar{R}, 0, 0$.

The joint at $\bar{R}, 0, 0$ was unique in that only type 1 nonorthogonal members intersected it. The joint orientation was taken as $\bar{R}, 0, 0$. If p_i represents the action components of a member in terms of the joint coordinate system and θ is the member orientation relative to the joint, then

$$\left. \begin{aligned} p'_1 &= p_1 \\ p'_2 &= p_2 \cos \theta - p_3 \sin \theta \\ p'_3 &= p_2 \sin \theta + p_3 \cos \theta \\ p'_4 &= p_4 \\ p'_5 &= p_5 \cos \theta - p_6 \sin \theta \\ p'_6 &= p_5 \sin \theta + p_6 \cos \theta \end{aligned} \right\} \quad (4)$$

The above relationships may be expressed more concisely as functions of the transformations discussed in appendix B:

$$\begin{pmatrix} p'_A \\ p'_B \end{pmatrix} = \begin{bmatrix} A_{0A} & 0 \\ 0 & I \end{bmatrix} \begin{pmatrix} p_A \\ p_B \end{pmatrix} \quad (5)$$

The forces at end A of the beam elements were rotated, and the forces at end B were premultiplied by the identity matrix only.

The assembly of the joint equilibrium equations was accomplished by the premultiplication of the matrix of member stiffnesses (expanded stiffness matrix) by a connection matrix. The matrix of member stiffnesses postmultiplied by the displacement vector yielded the actions on the beam. The use of a connection matrix is discussed in reference 6. The order of the resulting square matrix was reduced through the application of boundary conditions.

Two sources existed for the reduction of the unknowns prior to the solution of the set of joint equilibrium equations. These sources were boundary conditions and symmetry conditions. The displacement functions which describe an external support are fully described input quantities. For example, complete fixity of a joint may be realized by setting u_1 through $u_6 = 0$. A joint hinged along a circumferential line is known to have zero displacements in the u_1 through u_5 directions. Settlement of the external supports, that is, $u \neq 0$, is also a valid boundary condition. If elastic external supports are encountered, the spring rates of the supports would be required. The displacement u_1 in question would then be associated with the spring rates in the joint equilibrium equations.

Symmetry conditions may be separated into the following: (1) the special case of the joint at $\bar{R}, 0, 0$, and (2) the remaining joints on the diameter defining the mirror image boundary, that is, when $\theta = 0^\circ$. The mirror image symmetry was the result of a geometrical orientation of the capsule relative to the flight path in a manner similar to the orientation of an airplane to its flight path. In the special case (1), each beam of orientation $(\bar{R}, \varphi, \theta)$ occurred in company with a corresponding beam of orientation $(\bar{R}, \varphi, -\theta)$. The displacements at the plane of symmetry for both cases are

$$\left. \begin{array}{l} u_1 \neq 0 \\ u_2 \neq 0 \\ u_3 = 0 \\ u_4 = 0 \\ u_5 = 0 \\ u_6 \neq 0 \end{array} \right\} \quad (6)$$

Mechanical loads were introduced directly into the joint equilibrium equations. Distributed load systems were approximated by a set of concentrated loads applied at the joints. Equivalent joint loads were calculated from the reactions of the loaded fixed-ended beam elements.

The thermal gradient should be considered before discussing the calculation of the mechanically equivalent thermal loads. The temperatures of reentry vehicles of the type considered have the most significant gradient in the thickness direction of the ablator. This gradient may be approximated by dividing the ablator into several layers, each at a constant temperature, so that a step function results. It had been previously determined that the variation of temperature through the ablator thickness is parabolic, while the substrate temperature is essentially constant. The temperature of ablation is 1000° F .

The temperature of ablation determines the maximum temperature during re-entry. This temperature is not exceeded because of the formation of a char on the outer surface and because of the emission of cooling gases which limit the maximum temperature.

Figure 3 illustrates the temperature distribution through the thickness as represented by the approximating step function. The temperature in the i th layer of n layers is given by

$$T_i = T_s(\varphi, \theta) + \left[1000 - T_s(\varphi, \theta) \right] \left(\frac{i}{n} \right)^2 \quad (7)$$

The application of thermal loads was accomplished through a set of mechanically equivalent thermal loads. The loads were equal in magnitude but opposite in sense from the fixed-ended reactions of the thermally loaded beam element. These mechanically equivalent thermal loads were designated

$$p_{A0} = \left\{ \begin{array}{c} p_{A10} \\ p_{A20} \\ p_{A30} \\ p_{A40} \\ p_{A50} \\ p_{A60} \end{array} \right\} \quad (8)$$

and

$$p_{B0} = \left\{ \begin{array}{c} p_{B10} \\ p_{B20} \\ p_{B30} \\ p_{B40} \\ p_{B50} \\ p_{B60} \end{array} \right\} \quad (9)$$

The mechanically equivalent thermal loads at a joint were the sum of the fixed-ended actions of all the thermally loaded curved beams entering the joint. The solution of a thermally loaded curved beam was divided into two load conditions; (1) that due to uniform thermal strain, and (2) the nonuniform strain associated with thermal moment. The thermal moment at end B due to nonuniform thermal strain of type 1 and type 3 beams was designated

$$p_{B60} = b_{\varphi} \gamma_1 \quad (10)$$

The restraint necessary to fix the ends of a type 1 or type 3 curved beam under uniform thermal strain is developed as follows: if end A is fixed, the thermal translations at the free end B (fig. 6) are

$$\left. \begin{aligned} u_{B10} &= \bar{R} (1 - \cos \varphi_{AB}) \gamma_2 \\ u_{B20} &= \bar{R} \sin \varphi_{AB} \gamma_2 \\ u_{B30} &= 0 \\ u_{B40} &= 0 \\ u_{B50} &= 0 \\ u_{B60} &= 0 \end{aligned} \right\} \quad (11)$$

The compatibility equations may be written through the use of the previously developed element flexibility submatrix f_{BB} and the above thermal displacements.

$$f_{BB} p_{B0} + u_{B0} = 0 \quad (12)$$

Solving for the desired thermal restraints at end A, it is found that

$$p_{B0} = -k_{BB} u_{B0} \quad (13)$$

since $f_{BB}^{-1} = k_{BB}$. In expanded notation, p_{B0} is

$$\begin{Bmatrix} p_{B10} \\ p_{B20} \\ p_{B30} \\ p_{B40} \\ p_{B50} \\ p_{B60} \end{Bmatrix} = -k_{BB} \bar{R} \gamma_2 \begin{Bmatrix} 1 - \cos \varphi_{AB} \\ \sin \varphi_{AB} \\ 0 \\ 0 \\ 0 \\ 0 \end{Bmatrix} \quad (14)$$

The moment $b_{\varphi} \gamma_1$, described in equation (10) for the nonuniform thermal strain, must be superimposed on the above p_{B60} value which was necessary to maintain the conditions of fixity under a uniform thermal strain. The loads at end A of type 1 and type 3 beams are related to those defined for end B as follows:

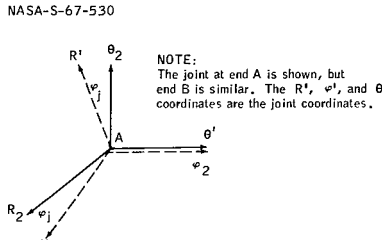
$$\begin{Bmatrix} p_{A10} \\ p_{A20} \\ p_{A30} \\ p_{A40} \\ p_{A50} \\ p_{A60} \end{Bmatrix} = \begin{Bmatrix} p_{B10} \\ -p_{B20} \\ p_{B30} \\ p_{B40} \\ p_{B50} \\ -p_{B60} \end{Bmatrix} \quad (15)$$

The mechanically equivalent thermal loads from type 2 and type 4 beams may be similarly defined in terms of the joint coordinates as

$$\begin{Bmatrix} p_{B10} \\ p_{B20} \\ p_{B30} \\ p_{B40} \\ p_{B50} \\ p_{B60} \end{Bmatrix} = \bar{R} \gamma_2 {}^A B'B^{-k} {}_{BB} \begin{Bmatrix} 1 - \cos \theta_{AB} \\ \sin \theta_{AB} \\ 0 \\ 0 \\ 0 \\ 0 \end{Bmatrix} + b_{\theta} \gamma_1 {}^A B'B \begin{Bmatrix} 0 \\ 0 \\ 0 \\ -\cos \varphi_j \\ 0 \\ \sin \varphi_j \end{Bmatrix} \quad (16)$$

where \bar{R} is $\bar{R} \sin \varphi_j$ for type 2 and type 4 beams. The thermal loads were developed in the coordinate system of figure 7 and then transformed through premultiplication by ${}^A B'B$. The mechanically equivalent actions occurring at end A of the beam are

NASA-S-67-530



NOTE:
The joint at end A is shown, but end B is similar. The R_1 , φ_1 , and θ_1 coordinates are the joint coordinates.

$$\begin{Bmatrix} p_{A10} \\ p_{A20} \\ p_{A30} \\ p_{A40} \\ p_{A50} \\ p_{A60} \end{Bmatrix} = \begin{Bmatrix} p_{B10} \\ p_{B20} \\ -p_{B30} \\ -p_{B40} \\ -p_{B50} \\ p_{B60} \end{Bmatrix} \quad (17)$$

Figure 7. - Joint and type 2 coordinate relationship.

The definition of the mechanically equivalent thermal loads has involved the use of two as yet undefined parameters. They are

$$\begin{aligned} \gamma_1 = & \sum_{i=1}^n \left(\frac{t_a}{n} \right)^2 \alpha_a E_a \left(\frac{\Delta R n}{t_a} + \frac{1}{2} - i - \frac{n t_b}{t_a} \right) (T_o - T_i) \\ & + t_b \alpha_b E_b \left(\Delta R - \frac{t_b}{2} \right) (T_o - T_b) + t_{fp} \alpha_s E_s (2\Delta R + t_s) (T_o - T_s) \end{aligned} \quad (18)$$

and

$$\gamma_2 = \frac{\sum_{i=1}^n \frac{t_a}{n} \alpha_a E_a (T_o - T_i) + t_b E_b \alpha_b (T_o - T_b) + 2t_{fp} E_s \alpha_s (T_o - T_s)}{\sum_{i=1}^n \frac{t_a}{n} E_a + t_b E_b + 2t_{fp} E_s} \quad (19)$$

It should be noted that all laminates were temperature-dependent with respect to their mechanical properties and the coefficient of thermal expansion. The temperature of the i th laminate of n laminates has been previously described in this section. With reference to figure 6, it may be observed that the thermal restraint forces p_{20} had to be supplemented by a set of thermal shear restraint forces p_{10} (p_{30} , p_{40} , and p_{50} are equal to zero) in order to satisfy equilibrium. The set of thermal restraint forces for any beam element formed a self-equilibrated force system. The thermal moments p_{50} and p_{60} were obtained by summing the product of the axial restraint force on each laminate and the distance to the neutral axis.

EXAMPLE APPLICATIONS OF THE PROCEDURE

Solutions to example problems solved by the method presented in this report were compared with other work. A limited amount of test data was obtained on a torispherical shell which had been statically tested (ref. 8). A laminated spherical cap under cold-soak conditions was subjected to a closed-form analytical solution (ref. 9). A laminated spherical cap and a laminated torispherical shell were analyzed under various mechanical and thermal load conditions (ref. 9). Many grid patterns (for example, figs. 8 and 9) were used in the present research to establish convergent solutions. The specific example problems which were used in the correlation program are outlined in the following paragraphs. The results are discussed in the next section.

Example 1 - Shallow Spherical Cap Under Distributed Loading

The structure for this example was a shallow spherical segment of the Apollo aft heat shield which had a radius of 175.6 inches. The structure was composed of two 0.008-inch stainless-steel face sheets brazed to a stainless-steel honeycomb core. The core was 3/16-inch square cell of 0.0010-inch foil gage.

A static test was conducted in which a distributed loading was simulated over a torispherical shell that represented the Apollo aft heat-shield substructure (ref. 8). The loading simulated the maximum dynamic air loading during the launch phase. It

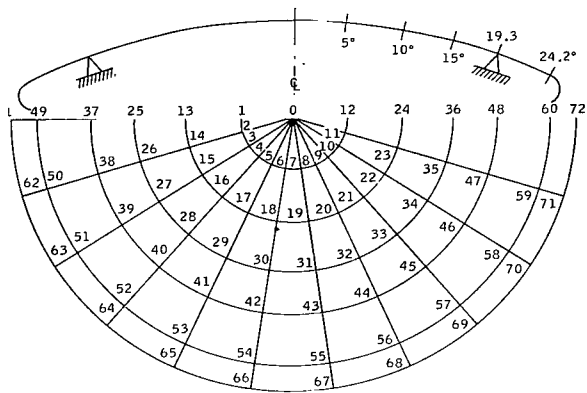


Figure 8. - Apollo aft heat-shield analysis using a 12, 6 grid pattern.

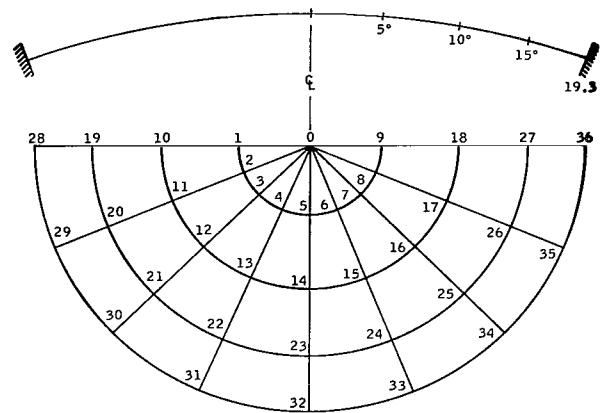


Figure 9. - Apollo aft heat-shield analysis using a 9, 4 grid pattern with the structure fixed at the bolt circle.

was assumed that the structure was fixed at the bolt circle (fig. 10). The bolt circle thus formed the boundary of a spherical cap. This spherical cap under distributed loading was analyzed using a finite-difference technique. An analysis of the same structure was performed under identical conditions using a finite-element technique (ref. 9). The two analytical solutions and the static test results are compared with results obtained from the method presented in this report.

Example 2 - Torispherical Shell Under Distributed Loading

The complete torispherical structure used in Apollo Test Request 209 (ATR-209, ref. 8) was supported at the bolt circle and at the torus. It was the same sandwich structure as was used in example 1. An analysis (ref. 9) of this structure under the ATR-209 loading condition was used for analytic correlation. The static test results are also included.

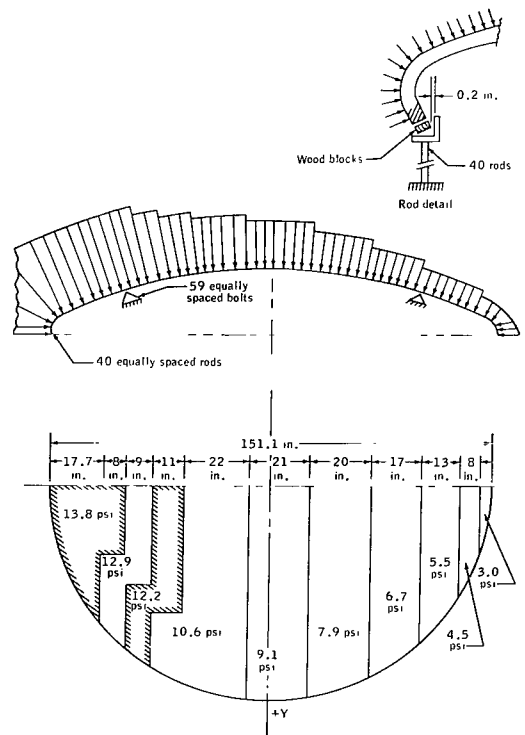


Figure 10. - ATR-209 pressure loading.

Example 3 - Torispherical Shell Under Water Impact

During the water landing of an Apollo command module, the torispherical shell is subjected to a pressure loading over a limited area. The extent of the area is a function of time (figs. 11 and 12), and is defined by the area of water in contact with the

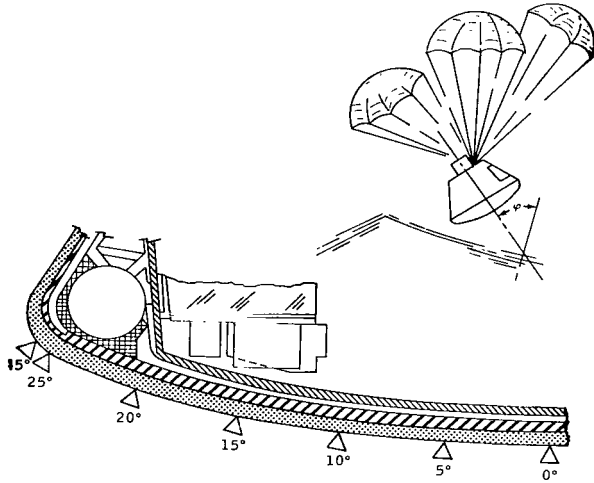
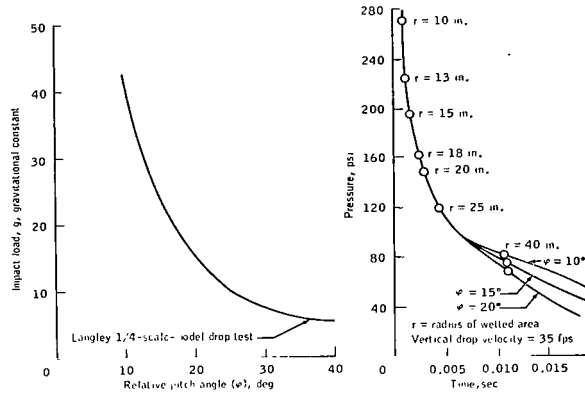


Figure 11. - Water impact landing, contact angle ϕ .



(a) Inertial loading.

(b) Water pressure.

Figure 12. - Water impact landing pressure.

spacecraft at any instant of time. The problem has many dynamic ramifications affecting the loading, stability, and structural response. This investigation was limited to the elastic analysis of the quasi-static structure.

Example 4 - Shallow Spherical Shell at -150° F

The same structure was used in example 4 as in example 1, but an ablator with a constant thickness of 1.84 inches was considered to be bonded to the substrate. The structure was subjected to a cold-soak (-150° F) thermal loading. A closed-form solution to this problem was reported in reference 9. Gallagher (ref. 9) also used his finite-element method to analyze the same structure under identical conditions. Both the closed-form and numerical-technique solutions were used for correlation purposes with results obtained from the present method.

Example 5 - Torispherical Shell at -150° F and at Reentry

The torispherical shell of example 2, with a variable thickness ablator, was exposed to two thermal load environments. The first was under the cold-soak (-150° F) conditions of example 4, which are representative of the translunar phase of spaceflight. The second thermal loading was a representative reentry hyperthermal load condition. In the performance of its function, the ablator limits the exterior temperature to the temperature of ablation (1000° F). The stainless-steel sandwich substrate had no

gradient and was always less than 600° F. The gradient through the ablator is parabolic from the 1000° F surface temperature to the temperature of the substrate. Gallagher (ref. 9) analyzed this problem using his finite-element method. The analytical results for the two thermal load conditions using the present method are correlated with the work of reference 9.

The spherical cap example problems and the spherical portion of the torispherical shells are actual representations of the substrate of the original Apollo aft heat shield. The torus area is composed of an outer shell backed up by corrugated ribs or "hat" sections. The present method was programed to accept basic laminate geometry and to convert these input data to the required stiffness parameters. Each laminate had its own moduli and mechanical properties, which were functions of material and temperature. It was convenient to introduce a structurally equivalent stainless-steel sandwich substrate in the torus area.

The temperature at which the composite laminated structure of example 4 and example 5 experienced zero stress was 185° F. The ablator was bonded to the substrate at a somewhat higher temperature, but a relaxation of stresses occurred during the curing cycle of the bond.

DISCUSSION OF RESULTS

The research described in this paper was applied to the five example structures discussed in the previous section. Comparisons of the results are discussed in this section.

Example 1 - Shallow Spherical Cap Under Distributed Loading

The displacement normal to the surface of the shallow spherical shell for the finite difference analysis, the reference 9 analysis, and the present analysis is presented in figure 13. The displacement values obtained agree more closely with the ATR-209 test values than the displacement values from either reference 8 or reference 9.

A comparison of meridional membrane stresses is presented in figure 14. The agreement among the analytical results is very good. Additionally, the stress at the apex ($\phi = 0$) obtained from the equation for hydrostatic loading (in ref. 10, Flügge points out that the stress in a shallow spherical shell under hydrostatic loading approaches the stress $\frac{PR}{2t}$ in areas away from the boundary) is in remarkable agreement at this point with the value from the present research. The differences between the recorded test values and the analytical values were never resolved, and some question remains as to the accuracy of the test values. This circumstance, combined with the observation that the three independent analyses are in close agreement, indicates a good possibility that the higher values are more reliable. The test data and the analytical data would align in a very satisfactory manner if the strain gage factor of 2.06 were applied to the test values from reference 7. This is also true of the meridional outside face sheet stresses shown in figure 15. It should be noted that the shape of the test data curve is the same as the author's analysis curve and that the 2.06 gage factor would again provide the desired alignment.

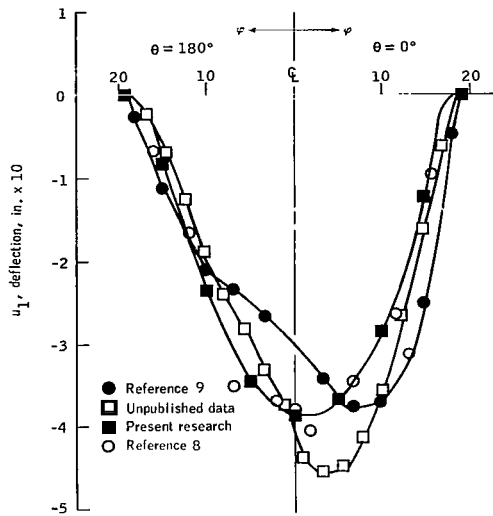


Figure 13. - ATR-209, u_1 displacement along axis of symmetry, fixed at bolt circle (unpublished data refers to a finite difference method).

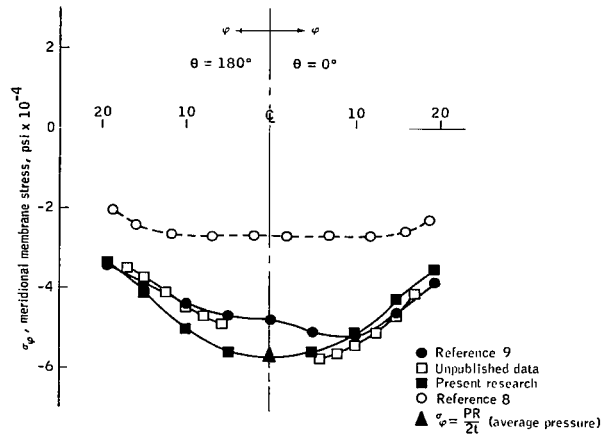


Figure 14. - ATR-209, comparison of meridional membrane stresses along diameter of symmetry (unpublished data refers to a finite difference method).

Example 2 - Torispherical Shell Under Distributed Loading

This example problem served primarily to demonstrate the convergence of the stiffness matrix solution presented in this paper. Many different grid patterns and grid densities were investigated. The stresses were compared previously in example 1 and were not significantly different in example 2. Thus, in reference 7 the convergence was discussed in terms of displacement relative to the shell surface.

Little discernible difference could be found in the various grid patterns. It was concluded that the method would yield satisfactory results for this structure without attendant convergence problems.

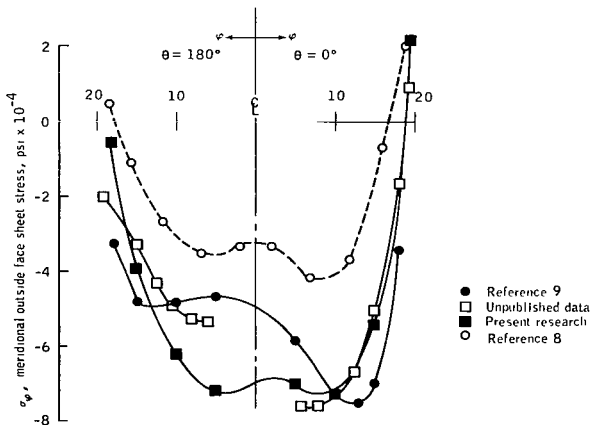


Figure 15. - ATR-209, comparison of meridional outside face sheet stresses along diameter of symmetry (unpublished data refers to a finite difference method).

Example 3 - Torispherical Shell Under Water Impact

The most severe loading of the Apollo aft heat-shield substructure occurs during the water landing. The critical internal loading is the R coordinate shear at the bolt circle. The command-module attitude just prior to impact is shown in figure 11. The effect of pitch angle φ on the impact loading and the relationships of pressure-time-wetted radii are illustrated in figure 12. A pseudostatic problem was defined by selecting a particular time after impact and noting the associated pressure-wetted radius shown in figure 12. A pitch angle of 15° and a wetted radius of 20 inches were run in the example (fig. 16). This condition occurs 0.003 second after impact, and there is a pressure of 150 psi over the circular area.

Critical values of shear occurred in the core at the bolt circle. Thus, in addition to a comparison of displacements normal to the surface (fig. 17), a comparison of core shear at the bolt circle was made (fig. 18). The displacement correlation with the

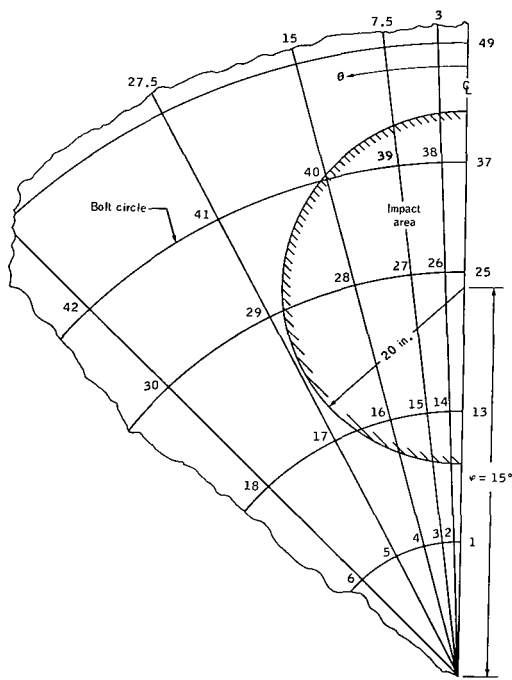


Figure 16. - Water impact area location relative to bolt circle of the Apollo aft heat shield.

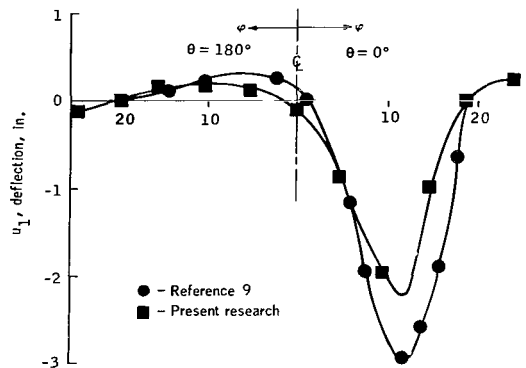


Figure 17. - Water impact, u_1 displacement along axis of symmetry of the Apollo aft heat shield.

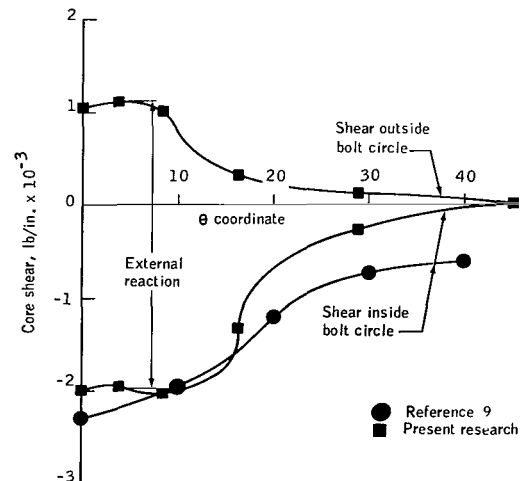


Figure 18. - Water impact, shear at the bolt circle of the Apollo aft heat shield.

results from reference 9 was fair. A comparison of the external reactions from reference 9 with the external reactions from the present research at the bolt circle was excellent. Difficulty was encountered when the internal stresses of the structural model were compared with those of the actual structure.

The support at the bolt circle of the actual structure is made up of 59 bolts, each spaced at 6.2 inches with a free span of less than 3 inches. The free-span distance from node point to node point along the bolt circle on the structural model was 16.4 inches. Circumferential shear occurred on the structural model which was known to be at variance with the actual structure. In the calculation of core shear, this circumferential shear was redistributed in the same proportion as the meridional core shear. The applied load is introduced at the node points, and a portion of the water-impact load must be placed at the support node points. Thus, it is necessary to introduce this portion of the core shear into the final core shear. Each joint was in equilibrium and this equilibrium was maintained in the resolution of the above factors to obtain core shear.

Example 4 - Shallow Spherical Shell at -150° F

A closed-form solution under cold-soak (-150° F) conditions of a shallow spherical cap of stainless-steel sandwich substrate covered with a 1.84-inch-thick ablator was reported in reference 9. The equations for the closed-form solution were derived in reference 9. The comparison of the displacement normal to the shell surface with comparable values by the present method was excellent (fig. 19). The displacement values of reference 9 were somewhat larger than the values obtained in the closed-form solution.

Example 5 - Torispherical Shell at -150° F and at Reentry

The comparison of u_1 displacements for the torispherical shell under cold-soak conditions is shown in figure 20. The values are uniformly less than those of the

NASA-S-67-536

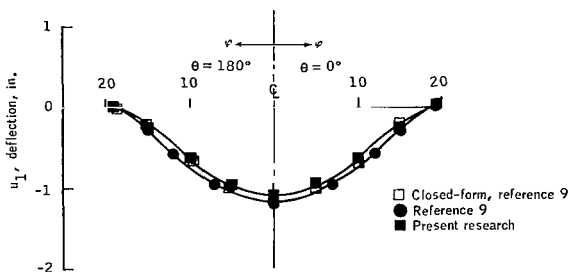


Figure 19. - Cold-soak condition, u_1 displacement along axis of symmetry of the Apollo aft heat shield (correlation with a closed-form solution).

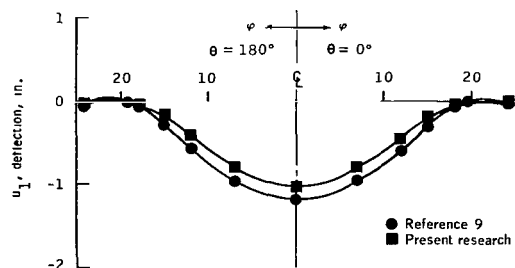


Figure 20. - Cold-soak condition, u_1 displacement along axis of symmetry of the Apollo aft heat shield.

analysis of reference 9. The correlation was considered to be satisfactory and compatible with the correlation shown in figure 19. The present analysis showed excellent agreement with the closed-form solution in figure 19. Consequently, it should be expected that the analysis of reference 9 would indicate a slightly more flexible structure.

A comparison of the φ normal stresses in the outside face of the ablator is shown in figure 21, while the φ normal stresses in the inner face sheet of the substrate obtained from the analyses of reference 9 and of the present research are illustrated in figure 22. The $E\alpha T$ actions are very dependent on grid size as they represent the fixed-ended conditions of a curved beam element under thermal loading. In the limit, as the grid size becomes more dense, the thermal stress would approach the value $E\alpha T$. It thus appears that satisfactory displacements are possible in thermal problems without a comparable correlation of stresses.

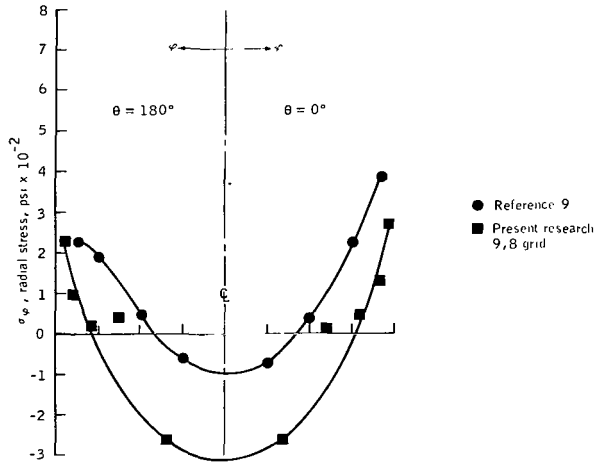


Figure 21.- Cold-soak condition, ablator normal stress in the φ direction along axis of symmetry of the Apollo aft heat shield.

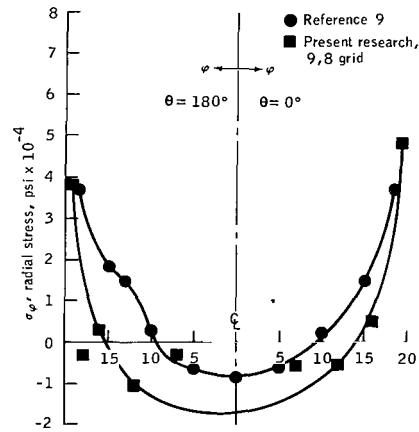


Figure 22.- Cold-soak condition, inner face sheet normal stress along axis of symmetry of the Apollo aft heat shield.

The displacements experienced during the reentry thermal loading were an order of magnitude less than those which occurred during the cold-soak (-150° F) thermal loading. Two different grid patterns were run to represent the analysis of the reentry case. The solutions were essentially identical (fig. 23); thus, a convergent solution was obtained for the present analysis. The larger percentage differences in this case between the results of the analysis of reference 9 and the present analysis are unexplained.

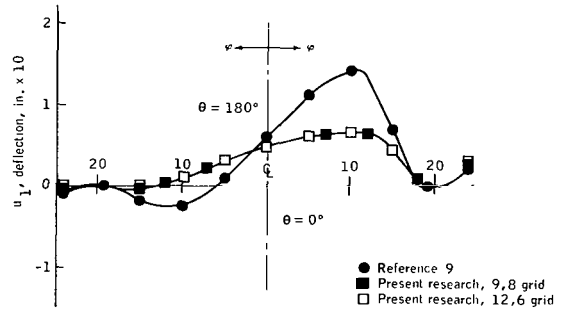


Figure 23.- Reentry condition, u_1 displacement along axis of symmetry of the Apollo aft heat shield.

RECOMMENDATIONS FOR FURTHER RESEARCH

There are several avenues of research which may be pursued to improve the procedure. These may be divided into three categories: (1) refinement of the theory, (2) application of the procedure to a greater variety of structures to determine the limitations of the procedure, and (3) more efficient use of the digital computer.

The coupling of the biaxial stresses has been mentioned earlier in this section. To effect a tractable solution, it was necessary to assume equal biaxial stresses in the sizing of the axial load-carrying capability of the typical beam elements. A possible approach to this problem would be first to assume equal stresses in the meridional and circumferential directions, and then to use the stresses obtained to size axial capability for a second solution. This process could be repeated until the desired accuracy was obtained.

It has been assumed that the change in geometry due to loading of the structure would have negligible effect on the solution. The influence of a generalized beam-column effect has been neglected. The improvement in the effectiveness of the program would be most noticeable in structures loaded near the buckling point. Thermal effects in reference 7 were limited to axial restraint and to restraint of the moment due to a temperature gradient through the thickness. The effect of the temperature variation in the shell midsurface was approximated in that each beam element was at a temperature constant in the φ and θ coordinates, but variable in the R coordinate. The temperature at any location on the structure was actually an approximation of a three-dimensional temperature variation, since the R variation in temperature was represented by multiple-stepped layers. Additional research could be directed toward more sophisticated thermal stress representation.

In the discussion of the results, it was noted that the thermal loads at the fixed ends of the beam elements are very dependent on grid size. Further research is recommended to seek a practical grid density at which this problem would diminish to engineering acceptance.

Curved beam elements were used in the present study. The displacement of the elastic axis due to a curved-beam effect was found to be negligible for the example structures (ref. 11) and was not included in this study. In structures which would require this consideration, the theory and computer programing are straightforward.

A modified von Karman membrane analogy was used to calculate the torsional capability of the beam elements in the present research. It is recommended that an experimental study of laminated composite beams be undertaken to improve the approach to torsional stiffness representation.

The exploration and extension of the program will have to be preceded by a learning period in which experience in the use of the computer program is attained. The good results experienced in the use of the present method on the Apollo aft heat-shield substructure were dependent on good structural idealization and realistic boundary conditions. The beam network may work satisfactorily for a wide range of shell structures, but this can only be determined through the application of the computer

program to many more structures than demonstrated by the example problems. Once the limitations of the computer program are understood and confidence in its use has been established, it would be possible to extend the program into the areas of linear elastic stability (ref. 12) and linearized plasticity (ref. 13). Both of these areas were outside the scope of the study presented in this report, but they are noteworthy directions in which further research would prove beneficial.

CONCLUSIONS

The stiffness matrix solution yielded highly satisfactory results for the Apollo aft heat-shield substructure. Success was achieved primarily because of the adequacy of the structural idealization. The frame networks of beam elements used to represent the shells of the example problems were demonstrated to be adequate for engineering purposes. Experience with the program will be required to establish the full range of structures which may be validly analyzed.

To effect tractable solutions of complex structures, it is necessary to make engineering compromises in all methods. The effect of Poisson's ratio was not completely accurate in the present report, but it was sufficiently accurate to obtain good engineering results. A plane stress condition was assumed in order that beam element stiffness matrices might be calculated; that is, the meridional and circumferential stresses were assumed equal so that the beam elements might be sized to reflect the Poisson effect. The use of concentrated loads to simulate a distributed load system could lead to difficulty if the grid size were too coarse. The assumption that the deformed geometry does not affect the solution ignores the effect of generalized beam-column action. Incorporation of this effect in linear elastic stability analysis has been accomplished by R. H. Gallagher and Joseph Padlog.

The attainment of a convergent solution for the Apollo aft heat shield was easily accomplished with coarse grid patterns. It is not expected that an indefinite refinement of the grid would lead to the "exact" solution. The adequacy of the beam elements to represent the idealized structure will break down in the limit. The use of extreme aspect ratios in the selection of grid patterns led to some difficulty in the satisfaction of equilibrium equations. This difficulty was not serious in the example problems but should be recognized. The limitations discussed did not adversely affect the structural analysis of the Apollo command module aft heat shield. It is concluded that composite shells of similar geometry and loadings may be successfully analyzed with engineering accuracy.

Manned Spacecraft Center
National Aeronautics and Space Administration
Houston, Texas, January 20, 1967
914-5020-01-72

APPENDIX A

FLEXIBILITY MATRIX

The details of the development of the flexibility matrix f_{BB} were not essential to the general development in the section on theory. Therefore, appendix A was designated for the derivation of f_{BB} .

Four structural elements were used in the analysis. It is emphasized that all elements were of the same structural type, that is, laminated beams. Each beam element was assumed to carry six generalized actions (three forces and three moments). The division into four types was necessary because of the variation in geometry of the example structures. The redefinition of geometry made it possible to use a single set of equations for all flexibility calculations. Type 1 and type 2 beams were on the sphere in the meridional and circumferential directions, respectively. Type 3 and type 4 beams were on the torus in the meridional and circumferential directions, respectively.

In the determination of the structural model, it was assumed that each beam element represented one-half of the area on either side of the beam. It was also assumed that the Poisson effect could be introduced into the present method through the modification of the C_1 terms. The bending stiffness was increased by $\frac{1}{1 - \nu^2}$ and the axial stiffness by $\frac{1}{1 - \nu}$.

The evaluation of the stiffness data is to a great extent self-explanatory; however, an explanation of the effect of temperature on the stiffness of the elements is in order. The specific treatment of the effect of temperature on the stiffness of the beam elements in the Apollo command module aft heat-shield substructure is discussed in this appendix; however, the discussion is applicable to a general class of composite shell structures. The composite nature of the structure is shown in the exploded view of figure 2. The steel sandwich substructure was at a constant temperature, but the ablator temperature varied in a parabolic manner from the temperature of ablation (1000° F) at the outside surface to a temperature T_b at the bond. The step-function approximation of temperature is shown in figure 3. In the range of temperatures encountered, the moduli of the steel substrate were not significantly affected. However, the small effect (approximately 10-percent reduction at 600° F from room temperature values) was incorporated into the computer program. The mechanical properties of the bond and ablative layers were very temperature-dependent. Their moduli and the

steel substrate moduli were represented in the computer program as polynomials in the temperature. The equation¹ for the modulus of rigidity of the core G_c was an empirical formulation, and is based on the gross cross section of the core. Hoff (ref. 14) presents a formal derivation of G_c but the results did not justify the increased complexity of its use.

In the calculation of the member stiffness, the composite nature of the structure made it necessary to associate each laminate with its correct moduli. The moduli were temperature-dependent and had to be considered in the calculation of the centroidal coordinate \bar{R} . The R coordinate to the outside face sheet was R_B , and the centroidal R coordinate (\bar{R}) was obtained by calculating the movement ΔR from R_B .

The moduli and geometry for the beam elements were obtained by averaging the terminal values, that is, the values at the joints. A discussion of the method used to obtain the torsional stiffness of the typical structural element appears at the end of this appendix.

Formation of Beam Element Flexibility Matrix, f_{BB}

$$f_{BB} = \begin{bmatrix} f_{B1, B1} & f_{B1, B2} & f_{B1, B3} & f_{B1, B4} & f_{B1, B5} & f_{B1, B6} \\ f_{B2, B1} & f_{B2, B2} & f_{B2, B3} & f_{B2, B4} & f_{B2, B5} & f_{B2, B6} \\ f_{B3, B1} & f_{B3, B2} & f_{B3, B3} & f_{B3, B4} & f_{B3, B5} & f_{B3, B6} \\ f_{B4, B1} & f_{B4, B2} & f_{B4, B3} & f_{B4, B4} & f_{B4, B5} & f_{B4, B6} \\ f_{B5, B1} & f_{B5, B2} & f_{B5, B3} & f_{B5, B4} & f_{B5, B5} & f_{B5, B6} \\ f_{B6, B1} & f_{B6, B2} & f_{B6, B3} & f_{B6, B4} & f_{B6, B5} & f_{B6, B6} \end{bmatrix} \quad (A1)$$

¹The equation for the modulus of rigidity of the core was developed by North American Aviation.

It was stated in the section on theory that the flexibility matrix f_{BB} would yield the stiffness matrix k_{BB} when inverted. The elements of f_{BB} were obtained through the use of the auxiliary load method (virtual work). The load diagrams resulting from the application of unit loads on a type 1 element AB, free at end B and fixed at end A, are shown in figure 5. These load expressions were inserted in the displacement equations of reference 6. As quoted from reference 6, the displacement is as follows:

$$u_r = \int_F n_r^x \times \frac{N^x dl}{EA^x} + \int_F n_r^y \times \frac{N^y dl}{GA^y} + \int_F n_r^z \times \frac{N^z dl}{GA^z} \\ + \int_F m_r^x \times \frac{M^x dl}{GI^x} + \int_F m_r^y \times \frac{M^y dl}{EI^y} + \int_F m_r^z \times \frac{M^z dl}{EI^z} \quad (A2)$$

where

A^x, A^y, A^z are the cross-sectional areas associated with the x, y, z actions

dl is the incremental length along the beam

E is the modulus of elasticity

G is the modulus of rigidity

I^x, I^y, I^z are the moments of inertia associated with the x, y, z actions

M^x is the twisting moment about the x -axis

M^y is the bending moment about the y -axis

M^z is the bending moment about the z -axis

N^x is the axial force in the x direction

N^y is the shear force in the y direction

N^z is the shear force in the z direction

n is the unit quantity of $N^x, N^y, N^z, M^x, M^y, M^z$ at r

u_r is the displacement at r

\int_F signifies integration around the whole frame

A summary of the flexibility equations appears in table A-I. The definition of the C_i expressions appearing in the table are shown later in this appendix.

Type 1 and Type 3 Members, C_i

$$C_1 = \frac{1 - \nu^2}{2EI_\theta} \quad (\text{A3a})$$

$$C_2 = \frac{1 - \nu^2}{2EI_R} \quad (\text{A3b})$$

$$C_3 = \frac{1}{2GJ_e} \quad (\text{A3c})$$

$$C_4 = \frac{1}{2GS_R} \quad (\text{A3d})$$

$$C_5 = \frac{1}{2GS_\theta} \quad (\text{A3e})$$

$$C_6 = \frac{1 - \nu}{2ES} \quad (\text{A3f})$$

$$C_7 = \varphi_{AB} \quad (\text{A3g})$$

$$C_8 = \sin \varphi_{AB} \quad (\text{A3h})$$

$$C_9 = \cos \varphi_{AB} \quad (\text{A3i})$$

$$C_{10} = \varphi_{AB} - \sin \varphi_{AB} \cos \varphi_{AB} = C_7 - C_8 C_9 \quad (\text{A3j})$$

$$C_{11} = \varphi_{AB} + \sin \varphi_{AB} \cos \varphi_{AB} = C_7 + C_8 C_9 \quad (\text{A3k})$$

$$C_{12} = 2 \cos \varphi_{AB} - 2 + \sin^2 \varphi_{AB} = 2C_9 - 2 + C_8^2 \quad (\text{A3l})$$

$$C_{13} = C_{11} + 2C_7 - 4C_8 \quad (\text{A3m})$$

$$C_{14} = C_{11} - 2C_8 \quad (\text{A3n})$$

$$C_{15} = 1 - C_9 \quad (\text{A3o})$$

$$C_{16} = C_8 - C_7 \quad (\text{A3p})$$

Type 1 and Type 3 Member Stiffness Data (See fig. 4)

$$\bar{R} = \Delta R + R_B \quad (\text{A4})$$

$$\Delta R = \frac{\left(\frac{t_a}{n}\right)^2 \sum_{i=1}^n \left[E_a(T_i) \left(n \frac{t_b}{t_a} + i - \frac{1}{2} \right) + E_b \frac{t_b^2}{2} - E_s \left[\frac{t_{fp}^2}{2} + t_{fp} \left(t_s - \frac{t_{fp}}{2} \right) \right] \right]}{\frac{t_a}{n} \sum_{i=1}^n E_a(T_i) + E_b t_b + 2E_s t_{fp}} \quad (\text{A5})$$

$$EI_\theta = \sum_{i=1}^n E_a(T_i) \frac{b}{12} \left(\frac{t_a}{n} \right)^3 + \sum_{i=1}^n E_a(T_i) b \frac{t_a}{n} \left(-\Delta R + t_b + \frac{it_a}{n} - \frac{t_a}{2n} \right)^2 + E_b b \frac{t_b}{2} \left(\frac{t_b}{2} - \Delta R \right)^2 + E_s \left[t_{fp} b \left(\Delta R + \frac{t_{fp}}{2} \right)^2 + t_{fp} b \left(t_s + \Delta R - \frac{t_{fp}}{2} \right)^2 \right] \quad (\text{A6})$$

$$EI_R = \frac{b^3 \varphi}{12} \left[\sum_{i=1}^n E_a (T_i) \frac{t_a}{n} + E_b t_b + 2E_s t_{fp} \right] \quad (A7)$$

$$G = \frac{E}{2(1 + \nu)} \quad (A8)$$

$$G_c = 2.43 \left(\frac{\rho'_c}{\rho_c} \right) G \quad 1.54 \quad (A9)$$

GJ_e (See section on calculation of torsional stiffness)

$$GS_R = b \varphi \left[\sum_{i=1}^n G_a (T_i) \frac{t_a}{n} + G_b t_b + G_c (t_s - 2t_{fp}) + 2G_s t_{fp} \right] \quad (A10)$$

$$GS_\theta = b \varphi \left[\sum_{i=1}^n G_a (T_i) \frac{t_a}{n} + G_b t_b + 2G_s t_{fp} \right] \quad (A11)$$

$$ES = b \varphi \left[\sum_{i=1}^n E_a (T_i) \frac{t_a}{n} + E_b t_b + 2E_s t_{fp} \right] \quad (A12)$$

Type 2 and Type 4 Members, C_i

$$C_1 = \frac{1 - \nu^2}{2EI_R} \quad (A13a)$$

$$C_2 = \frac{1 - \nu^2}{2EI_\varphi} \quad (A13b)$$

$$C_3 = \frac{1}{2GJ_e} \quad (A13c)$$

$$C_4 = \frac{1}{2GS_\varphi} \quad (\text{A13d})$$

$$C_5 = \frac{1}{2GS_R} \quad (\text{A13e})$$

$$C_6 = \frac{1 - \nu}{2ES} \quad (\text{A13f})$$

$$C_7 = \theta_{AB} \quad (\text{A13g})$$

$$C_8 = \sin \theta_{AB} \quad (\text{A13h})$$

$$C_9 = \cos \theta_{AB} \quad (\text{A13i})$$

$$C_{10} = \theta_{AB} - \sin \theta_{AB} \cos \theta_{AB} = C_7 - C_8 C_9 \quad (\text{A13j})$$

$$C_{11} = \theta_{AB} + \sin \theta_{AB} \cos \theta_{AB} = C_7 + C_8 C_9 \quad (\text{A13k})$$

$$C_{12} = 2 \cos \theta_{AB} - 2 + \sin^2 \theta_{AB} = 2C_9 - 2 + C_8^2 \quad (\text{A13l})$$

$$C_{13} = C_{11} + 2C_7 - 4C_8 \quad (\text{A13m})$$

$$C_{14} = C_{11} - 2C_8 \quad (\text{A13n})$$

$$C_{15} = 1 - C_9 \quad (\text{A13o})$$

$$C_{16} = C_8 - C_7 \quad (\text{A13p})$$

Type 2 and Type 4 Member Stiffness Data (See fig. 4)

$$EI_R = \frac{b_a^3}{12} \left[\sum_{i=1}^n E_a(T_i) \frac{t_a}{n} + E_b t_b + 2E_s t_{fp} \right] \quad (A14)$$

$$EI_\varphi = \sum_{i=1}^n E_a(T_i) \frac{b_\theta}{12} \left(\frac{t_a}{n} \right)^3 + \sum_{i=1}^n E_a(T_i) \frac{t_a}{n} b_\theta \left(-\Delta R + t_b + i \frac{t_a}{n} - \frac{t_a}{2n} \right)^2$$

$$+ E_b t_b b_\theta \left(\frac{t_b}{2} - \Delta R \right)^2 + E_s t_{fp} b_\theta \left[\left(\Delta R + \frac{t_{fp}}{2} \right)^2 + \left(t_s + \Delta R - \frac{t_{fp}}{2} \right)^2 \right] \quad (A15)$$

Note: Use ΔR as defined for type 1 beams.

$$G = \frac{E}{2(1 + \nu)} \quad (A16)$$

GJ_e (See section on the calculation of torsional stiffness)

$$GS_\varphi = b_\theta \left[\sum_{i=1}^n G_a(T_i) \frac{t_a}{n} + G_b t_b + 2G_s t_{fp} \right] \quad (A17)$$

$$GS_R = b_\theta \left[\sum_{i=1}^n G_a(T_i) \frac{t_a}{n} + G_b t_b + G_c (t_s - 2t_{fp}) + 2G_s t_{fp} \right] \quad (A18)$$

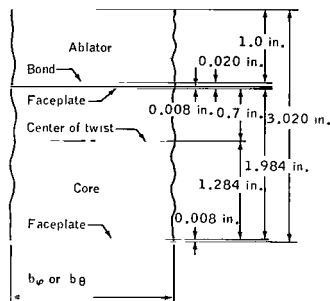
$$ES = b_\theta \left[\sum_{i=1}^n E_a(T_i) \frac{t_a}{n} + E_b t_b + 2E_s t_{fp} \right] \quad (A19)$$

Calculation of Torsional Stiffness

The conventional torsion formula is limited to circular cross sections. Prandtl developed a membrane analogy theory (ref. 15) for noncircular cross sections. This enables a valid use of the conventional torsion formula with the introduction of a geometric factor J_e . The modulus of rigidity G is constant throughout the cross section in the Prandtl theory. In the present application, the typical structural element was composed of a laminated rectangular cross section, with each laminate possessing an arbitrary modulus of rigidity. To account for the different moduli of the laminates, the modulus of rigidity of the gross cross section was taken to be proportional to (1) the laminate cross-sectional area, (2) the laminate modulus of rigidity, and (3) the distance from the center of twist in the direction of the shortest dimension of the cross section. This was compatible with the assumption of an equal angle of twist for all laminates in a cross section, and of a linear shear stress distribution across the shortest dimension (ref. 16). The foregoing may be expressed mathematically as

$$G_e = \frac{\sum_i G_i t_i d_i}{\sum_i t_i d_i} \quad (A20)$$

and its application to the Apollo command-module aft heat shield is found in figure A-1. The use of the equivalent modulus of rigidity G_e in the modified Prandtl theory follows.



$$G_e = \frac{\sum_i G_i t_i d_i}{\sum_i t_i d_i} = \frac{385\,909}{2.337624} = 165\,086$$

In reference 15

$$M_T = k_1 G \theta (2a)^3 2b \quad (A21)$$

or in the notation of the present research

$$p_5 = G_e k_1 \varphi (b \varphi)^3 \sum_i t_i \quad (A22)$$

Solving for φ , it is found that

$$\varphi = \frac{p_5}{G_e k_1 (b \varphi)^3 \sum_i t_i} \quad (\text{type 1 member}) \quad (A23)$$

Laminate	i	t_i in.	d_i in.	G_i psi	$t_i d_i$ in ²	$G_i t_i d_i$ lb
Ablator ^a	1	1	1.728	100 000	1.728	172 800
Bond	2	0.020	0.718	414 000	0.01436	5 945
Faceplate	3	0.008	0.704	12 000 000	0.005632	67 584
Core	4	1.984	0.292	27 500	0.579328	15 932
Faceplate	5	0.008	1.288	12 000 000	0.010304	123 648
$\Sigma \rightarrow$	-	-	-	-	2.337624	385 909

^aAblator may be multilayered for temperature dependence.

Figure A-1. - Example calculation of torsional stiffness.

A comparison with the well-known torsional formula $\varphi = \frac{T}{GJ_e}$ reveals $G_e J_e$ to equal $G_e k_1 (b_\varphi)^3 \sum_i t_i$. The constant k_1 is taken from reference 15 and is tabulated below.

$b_\varphi \sum_i t_i$	k_1
1.0	0.1406
1.2	0.166
1.5	0.196
2.0	0.229
2.5	0.249
3	0.263
4	0.281
5	0.291
10	0.312
∞	0.333

TABLE A-I. - SUMMARY OF DISPLACEMENT INFLUENCE COEFFICIENTS

\bar{R} used for type 1 and type 3 beams
 $\bar{R} \sin \varphi$ used for type 2 and type 4 beams

	1	2	3	4	5	6
1	$\bar{R}C_6C_{10}$ $+\bar{R}C_4C_{11}$ $+(\bar{R})^3C_1C_{10}$	$\bar{R}C_6C_8^2$ $-\bar{R}C_4C_8^2$ $+(\bar{R})^3C_1C_{12}$	0	0	0	$-2(\bar{R})^2C_1C_{15}$
2	$\bar{R}C_6C_8^2$ $-\bar{R}C_4C_8^2$ $+(\bar{R})^3C_1C_{12}$	$\bar{R}C_6C_{11}$ $+\bar{R}C_4C_{10}$ $+(\bar{R})^3C_1C_{13}$	0	0	0	$-2(\bar{R})^2C_1C_{16}$
3	0	0	$2\bar{R}C_5C_7$ $+(\bar{R})^3C_3C_{13}$ $+(\bar{R})^3C_2C_{10}$	$-(\bar{R})^2C_3C_{12}$ $+(\bar{R})^2C_2C_8^2$	$-(\bar{R})^2C_3C_{14}$ $-(\bar{R})^2C_2C_{10}$	0
4	0	0	$-(\bar{R})^2C_3C_{12}$ $+(\bar{R})^2C_2C_8^2$	$\bar{R}C_3C_{10}$ $+\bar{R}C_2C_{11}$	$\bar{R}C_3C_8^2$ $-\bar{R}C_2C_8^2$	0
5	0	0	$-(\bar{R})^2C_3C_{14}$ $-(\bar{R})^2C_2C_{10}$	$\bar{R}C_3C_8^2$ $-\bar{R}C_2C_8^2$	$\bar{R}C_3C_{11}$ $+\bar{R}C_2C_{10}$	0
6	$-2(\bar{R})^2C_1C_{15}$	$-2(\bar{R})^2C_1C_{16}$	0	0	0	$2\bar{R}C_1C_7$

APPENDIX B

TRANSFORMATION MATRICES

A congruent transformation was used to obtain the total member stiffness matrix once the stiffness submatrix k_{BB} was obtained from the inversion of the flexibility matrix f_{BB} . A typical type 1 beam element is shown in figure 6. A system of displacements u_B induced actions p_{BB} at end B and p_{AB} at end A, such that

$$p_{BB} = k_{BB}u_B \quad (B1)$$

$$p_{AB} = k_{AB}u_B \quad (B2)$$

The actions p_{BB} were expressed in the axes at end B, while actions p_{AB} were expressed in the axes at end A. These two sets of actions formed a system of equilibrium equations acting on the member AB. If the actions p_{BB} are transformed to the axes at end A, the equilibrium equations are

$$p_{AB} + A_{AB}p_{BB} = 0 \quad (B3)$$

and thus

$$p_{AB} = -A_{AB}p_{BB} \quad (B4)$$

Therefore

$$k_{AB}u_B = -A_{AB}k_{BB}u_B \quad (B5)$$

and

$$k_{AB} = -A_{AB}k_{BB} \quad (B6)$$

Similarly

$$k_{BA} = -A_{BA}k_{AA} \quad (B7)$$

The stiffnesses k_{AA} and k_{BB} are also related to one another. From the reciprocal law it is known that $k_{BA} = k'_{AB}$, thus

$$-A_{BA}k_{AA} = \left(-A_{AB}k_{BB}\right)' \quad (B8)$$

Since the transpose of the product of two matrices is equal to the product of their transposes in reverse order

$$-A_{BA}k_{AA} = -k'_{BB}A'_{AB} \quad (B9)$$

and

$$k_{AA} = A_{BA}^{-1}k'_{BB}A'_{AB} \quad (B10)$$

Since

$$A_{BA}^{-1} = A_{AB} \quad (B11)$$

and

$$k_{BB} = k'_{BB} \quad (B12)$$

$$k_{AA} = A_{AB}k_{BB}A'_{AB} \quad (B13)$$

The above submatrix stiffness definitions may be collected into a single matrix expression for the actions on the member AB in terms of the end displacements u_A and u_B .

$$\begin{Bmatrix} p_A \\ p_B \end{Bmatrix} = \begin{bmatrix} k_{AA} & k_{AB} \\ k_{BA} & k_{BB} \end{bmatrix} \begin{Bmatrix} u_A \\ u_B \end{Bmatrix} \quad (\text{B14a})$$

$$\begin{Bmatrix} p_A \\ p_B \end{Bmatrix} = \begin{bmatrix} A_{AB} & k_{BB} & A'_{AB} & -A_{AB} & k_{BB} \\ -k_{BB} & A'_{AB} & & & k_{BB} \end{bmatrix} \begin{Bmatrix} u_A \\ u_B \end{Bmatrix} \quad (\text{B14b})$$

A similar approach was used in the calculation of f_{BB} for type 2 beam elements. An additional congruent transformation was required to orient the forces and displacements with the joint orientation. The relationship of the coordinates in the type 2 beam formulas to the joint coordinates is shown in figure 7. The transformation matrix manipulation follows.

$$\begin{Bmatrix} p_A \\ p_B \end{Bmatrix} = \begin{bmatrix} k_{AA} & k_{AB} \\ k_{BA} & k_{BB} \end{bmatrix} \begin{Bmatrix} u_A \\ u_B \end{Bmatrix} \quad (\text{B15})$$

$$\begin{Bmatrix} p_{A'} \\ p_{B'} \end{Bmatrix} = \begin{bmatrix} A_{A'A} & 0 \\ 0 & A_{B'B} \end{bmatrix} \begin{bmatrix} k_{AA} & k_{AB} \\ k_{BA} & k_{BB} \end{bmatrix} \begin{Bmatrix} u_A \\ u_B \end{Bmatrix} \quad (\text{B16})$$

$$\begin{Bmatrix} p_{A'} \\ p_{B'} \end{Bmatrix} = \begin{bmatrix} A_{A'A} & k_{AA} & A_{A'A} & k_{AB} \\ A_{B'B} & k_{BA} & A_{B'B} & k_{BB} \end{bmatrix} \begin{Bmatrix} u_A \\ u_B \end{Bmatrix} \quad (\text{B17})$$

$$\begin{Bmatrix} p_{A'} \\ p_{B'} \end{Bmatrix} = \begin{bmatrix} A_{A'A} & k_{AA} & A_{A'A} & k_{AB} \\ A_{B'B} & k_{BA} & A_{B'B} & k_{BB} \end{bmatrix} \begin{bmatrix} A_{A'A} & 0 \\ 0 & A_{B'B} \end{bmatrix} \begin{Bmatrix} u_{A'} \\ u_{B'} \end{Bmatrix} \quad (\text{B18})$$

$$\begin{Bmatrix} p_{A'} \\ p_{B'} \end{Bmatrix} = \begin{bmatrix} A_{A'A} & k_{AA} & A'_{A'A} & A_{A'A} & k_{AB} & A'_{B'B} \\ A_{B'B} & k_{BA} & A'_{A'A} & A_{B'B} & k_{BB} & A'_{B'B} \end{bmatrix} \begin{Bmatrix} u_{A'} \\ u_{B'} \end{Bmatrix} \quad (\text{B19})$$

The type 1 beams which meet at the apex required an additional congruent transformation of actions and displacements to make each compatible with the single set of joint coordinates at zero. The zero joint is oriented such that the local φ coordinate makes an angle of 0° with the θ coordinate of the fixed reference point of the shell. This is illustrated as

$$\begin{Bmatrix} p_A \\ p_B \end{Bmatrix} = \begin{bmatrix} k_{AA} & k_{AB} \\ k_{BA} & k_{BB} \end{bmatrix} \begin{Bmatrix} u_A \\ u_B \end{Bmatrix} \quad (\text{B20})$$

Transform actions at end A to the zero joint orientation

$$\begin{Bmatrix} p_{0A} \\ p_B \end{Bmatrix} = \begin{bmatrix} A_{0A} & 0 \\ 0 & I \end{bmatrix} \begin{bmatrix} k_{AA} & k_{AB} \\ k_{BA} & k_{BB} \end{bmatrix} \begin{Bmatrix} u_A \\ u_B \end{Bmatrix} \quad (\text{B21})$$

$$\begin{Bmatrix} p_{0A} \\ p_B \end{Bmatrix} = \begin{bmatrix} A_{0A} & k_{AA} & A_{0A} & k_{AB} \\ & k_{BA} & & k_{BB} \end{bmatrix} \begin{Bmatrix} u_A \\ u_B \end{Bmatrix} \quad (\text{B22})$$

Then transform the displacements at end A to the zero joint orientation

$$\begin{Bmatrix} p_{0A} \\ p_B \end{Bmatrix} = \begin{bmatrix} A_{0A} & k_{AA} & A_{0A} & k_{AB} \\ k_{BA} & & k_{BB} & \end{bmatrix} \begin{bmatrix} A'_{0A} & 0 \\ 0 & I \end{bmatrix} \begin{Bmatrix} u_{0A} \\ u_B \end{Bmatrix} \quad (\text{B23})$$

$$\begin{Bmatrix} p_{0A} \\ p_B \end{Bmatrix} = \begin{bmatrix} A_{0A} & k_{AA} & A'_{0A} & A_{0A} & k_{AB} \\ k_{BA} & A'_{0A} & & k_{BB} & \end{bmatrix} \begin{Bmatrix} u_{0A} \\ u_B \end{Bmatrix} \quad (\text{B24})$$

The calculation of the thermal load vector required rotational transformations for all type 2 beam elements and those type 1 beam elements common to the apex. The use of the required transformations is as follows:

Type 1 beam elements

$$\begin{Bmatrix} p_{0A} \\ p_B \end{Bmatrix} = \begin{bmatrix} A_{0A} & 0 \\ 0 & I \end{bmatrix} \begin{Bmatrix} p_A \\ p_B \end{Bmatrix} \quad (\text{B25})$$

Type 2 beam elements

$$\begin{Bmatrix} p_{1A} \\ p_{1B} \end{Bmatrix} = \begin{bmatrix} A_{A'A} & 0 \\ 0 & A_{B'B} \end{bmatrix} \begin{Bmatrix} p_{2A} \\ p_{2B} \end{Bmatrix} \quad (\text{B26})$$

The transformations discussed above required the use of special transformation matrices. These matrices are developed in detail in reference 7.

REFERENCES

1. Radkowski, P. P. ; Davis, R. M. ; and Bolduc, M. R. : Numerical Analysis of Equations of Thin Shells of Revolution. ARS J., vol. 32, no. 1, Jan. 1962, pp. 36-41.
2. Sepetoski, W. K. ; Pearson, C. E. ; Dingwell, I. W. ; and Adkins, A. W. : A Digital Computer Program for the General Axially Symmetric Thin-Shell Problem. J. Appl. Mech., vol. 29, no. 4, Dec. 1962, pp. 655-661.
3. Steele, C. R. ; and Hartung, R. F. : Symmetric Loading of Orthotropic Shells of Revolution. J. Appl. Mech., vol. 32, no. 2, June 1965, pp. 337-345.
4. Cohen, G. A. : Computer Analysis of Asymmetrical Deformation of Orthotropic Shells of Revolution. AIAA, vol. 2, no. 5, May 1964, pp. 932-934.
5. Radkowski, P. P. : Stress Analysis of Orthotropic Thin Multilayer Shells of Revolution. Preprint 2889-63, AIAA, Apr. 1963.
6. Hall, A. S. ; and Woodhead, R. W. : Frame Analysis. John Wiley & Sons, Inc., 1961.
7. Stebbins, Frederick Jean: Stiffness Matrix Solution for Shells of Revolution Possessing Variable Thickness Heat Protection. Ph. D. Dissertation, Texas A&M Univ., 1966.
8. Shackett, J. M. : Structural Test Report on the Command Module Aft Heat Shield Substructure and Aft Section of the Inner Structure (ATR 209-1 & -2). SID 65-358, North American Aviation, Inc., March 1965.
9. Gallagher, R. H. ; Gellatly, R. A. ; and Batt, J. R. : Structural and Dynamic Analysis of the Apollo Aft Heat Shield. Report No. D 7218-933004, Bell Aerosystems Company, Dec. 1965.
10. Flügge, Wilhelm: Stresses in Shells. Springer-Verlag, Berlin/Göttingen/Heidelberg, 1960.
11. Roark, Raymond J. : Formulas for Stress and Strain. Third ed., McGraw-Hill Book Co., Inc., 1954.
12. Gallagher, R. H. ; and Padlog, Joseph: Discrete Element Approach to Structural Instability Analysis. AIAA, vol. 1, no. 6, June 1963, pp. 1437-1439.
13. Phillips, Aris: Introduction to Plasticity. The Ronald Press Company, N. Y., 1956.
14. Hoff, Nicholas J. : The Analysis of Structures. John Wiley & Sons, Inc., 1956.

15. Timoshenko, S.; and Goodier, J. N.: Theory of Elasticity. Second ed., McGraw-Hill Book Co., Inc., 1951.

16. Shanley, F. R.: Strength of Materials. McGraw-Hill Book Co., Inc., 1957.

"The aeronautical and space activities of the United States shall be conducted so as to contribute . . . to the expansion of human knowledge of phenomena in the atmosphere and space. The Administration shall provide for the widest practicable and appropriate dissemination of information concerning its activities and the results thereof."

—NATIONAL AERONAUTICS AND SPACE ACT OF 1958

NASA SCIENTIFIC AND TECHNICAL PUBLICATIONS

TECHNICAL REPORTS: Scientific and technical information considered important, complete, and a lasting contribution to existing knowledge.

TECHNICAL NOTES: Information less broad in scope but nevertheless of importance as a contribution to existing knowledge.

TECHNICAL MEMORANDUMS: Information receiving limited distribution because of preliminary data, security classification, or other reasons.

CONTRACTOR REPORTS: Scientific and technical information generated under a NASA contract or grant and considered an important contribution to existing knowledge.

TECHNICAL TRANSLATIONS: Information published in a foreign language considered to merit NASA distribution in English.

SPECIAL PUBLICATIONS: Information derived from or of value to NASA activities. Publications include conference proceedings, monographs, data compilations, handbooks, sourcebooks, and special bibliographies.

TECHNOLOGY UTILIZATION PUBLICATIONS: Information on technology used by NASA that may be of particular interest in commercial and other non-aerospace applications. Publications include Tech Briefs, Technology Utilization Reports and Notes, and Technology Surveys.

Details on the availability of these publications may be obtained from:

SCIENTIFIC AND TECHNICAL INFORMATION DIVISION
NATIONAL AERONAUTICS AND SPACE ADMINISTRATION
Washington, D.C. 20546